

Cosmic Structure as the Quantum Interference of a Coherent Dark Wave

Hsi-Yu Schive¹, Tzihong Chiueh^{1,2*} & Tom Broadhurst^{3,4}

chiuehth@phys.ntu.edu.tw

The conventional cold, particle interpretation of dark matter (CDM) still lacks laboratory support and struggles with the basic properties of common dwarf galaxies, which have surprisingly uniform central masses and shallow density profiles^{1–4}. In contrast, galaxies predicted by CDM extend to much lower masses, with steeper, singular profiles^{5–7}. This tension motivates cold, wavelike dark matter (ψ DM) composed of a non-relativistic Bose-Einstein condensate, so the uncertainty principle counters gravity below a Jeans scale^{8,9}. Here we achieve the first cosmological simulations of this quantum state at unprecedentedly high resolution capable of resolving dwarf galaxies, with only one free parameter, m_B , the boson mass. We demonstrate the large scale structure of this ψ DM simulation is indistinguishable from CDM, as desired, but differs radically inside galaxies. Connected filaments and collapsed haloes form a large interference network, with gravitationally self-bound solitonic cores inside every galaxy surrounded by extended haloes of fluctuating density granules. These results allow us to determine $m_B = (8.1^{+1.6}_{-1.7}) \times 10^{-23}$ eV using stellar phase-space distributions in dwarf spheroidal galaxies. Denser, more massive solitons are predicted for Milky Way sized galaxies, providing a substantial seed to help explain early spheroid formation. Suppression of small structures means the onset of galaxy formation for ψ DM is substantially delayed relative to CDM, appearing at $z \lesssim 13$ in our simulations.

Thermally produced particle candidates for the dark matter are still without laboratory support, including those favoured by super-symmetric theories in the TeV range. Non-thermal bosonic fields, particularly scalar fields, provide another well motivated class of dark matter, formed in a non-relativistic, low-momentum state as a cold Bose-Einstein condensate (BEC), and increasingly motivated by extensions of the Standard Model of particle physics and

to the mechanism driving the universal expansion¹⁰. The field in this context can be described by a coherent wave function ψ with an interference pattern determining the distribution of dark matter, which we term ψ DM. Axion is a long-standing CDM candidate of this form, and higher dimensional theories motivate an “axiverse”, where a discrete mass spectrum of axion-like particles spans many decades, possibly affecting cosmic structure¹¹.

The distribution of ψ DM mimics particle CDM on large scales^{13–15}, and hence distinguishing between CDM and cold, wavelike ψ DM is best made on small scales due to the additional quantum stress^{8,9,15}. Dwarf spheroidal (dSph) galaxies are the smallest and most common class of galaxy with internal motions dominated by dark matter. Their basic properties are very hard to explain with standard

¹Dept. of Physics, National Taiwan Univ., Taipei 10617, Taiwan

²Center for Theoretical Sciences, National Taiwan Univ., Taipei 10617, Taiwan

³Dept. of Theoretical Physics, Univ. of the Basque Country UPV/EHU, E-48080 Bilbao, Spain

⁴Ikerbasque, Basque Foundation for Science, E-48011 Bilbao, Spain

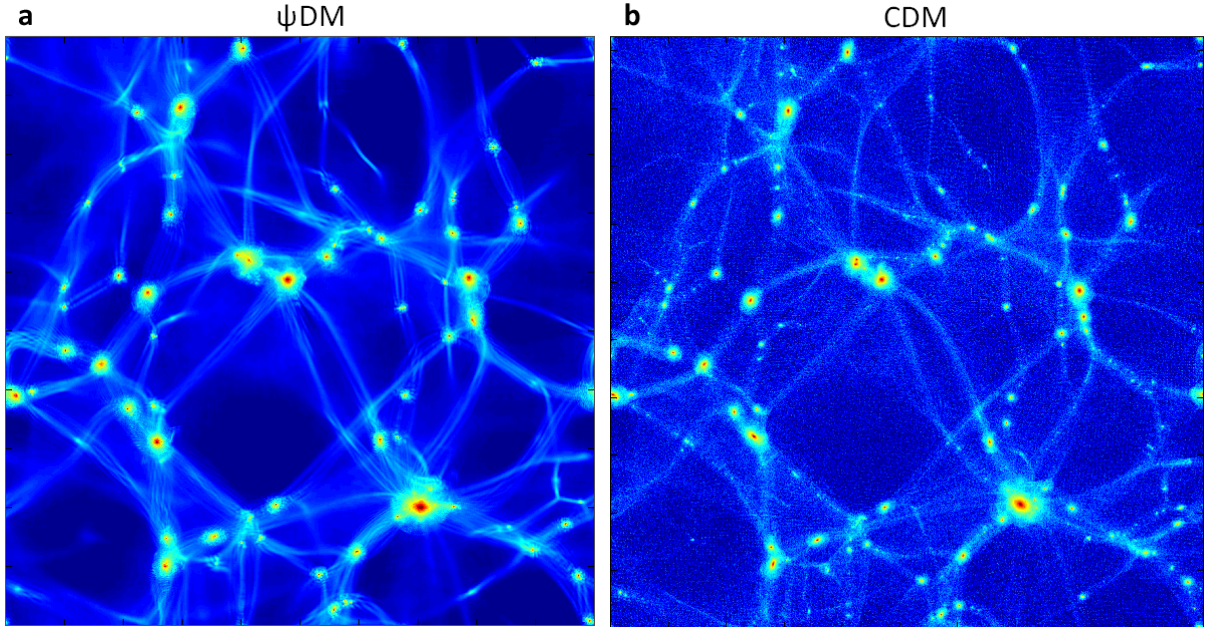


Figure 1: Comparison of cosmological large-scale structures formed by standard CDM and by wave-like dark matter, ψ DM. Panel (a) shows the structure created by evolving a single coherent wave function for $\Lambda\psi$ DM calculated on AMR grids. Panel (b) is the structure simulated with a standard Λ CDM N-body code GADGET-2¹² for the same cosmological parameters, with the high-k modes of the linear power spectrum intentionally suppressed in a way similar to the ψ DM model to highlight the comparison of large-scale features. This comparison clearly demonstrates that the large scale distribution of filaments and voids is indistinguishable between these two completely different calculations, as desired given the success of Λ CDM in describing the observed large scale structure. ψ DM arises from the low momentum state of the condensate so that it is equivalent to collisionless CDM well above the Jeans scale.

CDM, including the surprising uniformity of their central masses, $M(< 300 \text{ pc}) \simeq 10^7 M_\odot$, and shallow density profiles^{1–4}. In contrast, galaxies predicted by CDM extend to much lower masses, well below the observed dwarf galaxies, with steeper, singular mass profiles^{5–7}. Adjustments to standard CDM addressing these difficulties consider particle collisions¹⁶, or warm dark matter (WDM)¹⁷. WDM can be tuned to suppress small scale structures, but does not provide large enough flat cores^{18,19}. Collisional CDM can be adjusted to generate flat cores, but cannot suppress low mass galaxies without resorting to other baryonic physics²⁰. Better agreement is expected for ψ DM because the uncertainty principle counters gravity below a Jeans scale, simultaneously suppressing small scale structures and limiting the central density of collapsed haloes^{8,9}.

Detailed examination of structure formation with ψ DM is therefore highly desirable, but, unlike the extensive N-body investigation of standard

CDM, no sufficiently high resolution simulations of ψ DM have been attempted. The wave mechanics of ψ DM can be described by Schrödinger’s equation, coupled to gravity via Poisson’s equation¹³ with negligible microscopic self-interaction. The dynamics here differs from collisionless particle CDM by a new form of stress tensor from quantum uncertainty, giving rise to a comoving Jeans length, $\lambda_J \propto (1+z)^{1/4} m_B^{-1/2}$, during the matter-dominated epoch¹⁵. The insensitivity of λ_J to redshift, z , generates a sharp cutoff mass below which structures are suppressed. Cosmological simulations in this context turn out to be much more challenging than standard N-body simulations as the highest frequency oscillations, ω , given approximately by the matter wave dispersion relation, $\omega \propto m_B^{-1} \lambda^{-2}$, occur on the smallest scales, requiring very fine temporal resolution even for moderate spatial resolution (see Supplementary Fig. S1). In this work, we optimise an adaptive-mesh-refinement (AMR) scheme, with

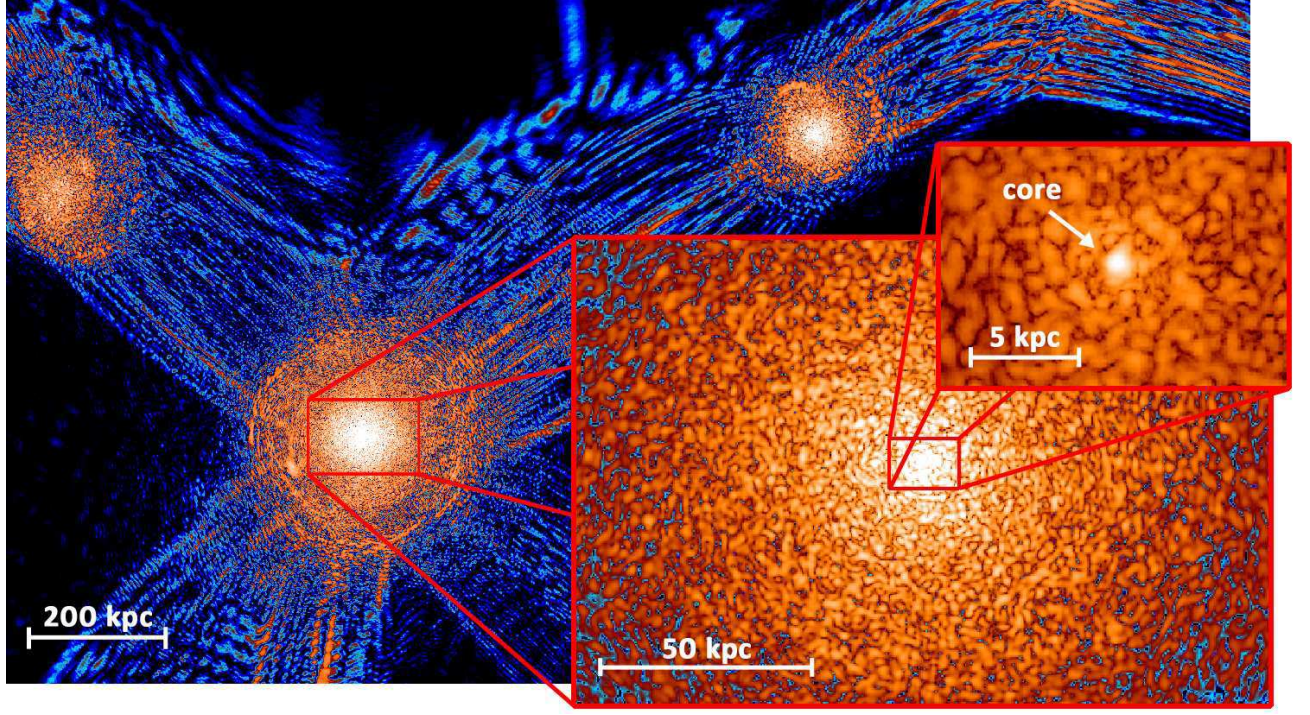


Figure 2: A slice of density field of ψ DM simulation on various scales at $z = 0.1$. This scaled sequence (each of thickness 60 pc) shows how quantum interference patterns can be clearly seen everywhere from the large-scale filaments, tangential fringes near the virial boundaries, to the granular structure inside the haloes. Distinct solitonic cores with radius $\sim 0.3 - 1.6$ kpc are found within each collapsed halo. The density shown here spans over nine orders of magnitude, from 10^{-1} to 10^8 (normalized to the cosmic mean density). The color map scales logarithmically, with cyan corresponding to density $\lesssim 10$.

graphic processing unit acceleration, improving performance by almost two orders of magnitude²¹ (see Supplementary Section 1 for details).

Fig. 1 demonstrates that despite the completely different calculations employed, the pattern of filaments and voids generated by a conventional N-body particle Λ CDM simulation is remarkably indistinguishable from the wavelike $\Lambda\psi$ DM for the same linear power spectrum (see Supplementary Fig. S2). Here Λ represents the cosmological constant. This agreement is desirable given the success of standard Λ CDM in describing the statistics of large scale structure. To examine the wave nature that distinguishes ψ DM from CDM on small scales, we resimulate with a very high maximum resolution of 60 pc for a 2 Mpc comoving box, so that the densest objects formed of $\gtrsim 300$ pc size are well resolved with $\sim 10^3$ grids. A slice through this box is shown in Fig. 2, revealing fine interference fringes defining long filaments, with tangential fringes near

the boundaries of virialized objects, where the de Broglie wavelengths depend on the local velocity of matter. An unexpected feature of our ψ DM simulations is the generation of prominent dense coherent standing waves of dark matter in the center of every gravitational bound object, forming a flat core with a sharp boundary (Figs. 2 and 3). These dark matter cores grow as material is accreted and are surrounded by virialized haloes of material with fine-scale, large-amplitude cellular interference, which continuously fluctuates in density and velocity generating quantum and turbulent pressure support against gravity.

The central density profiles of all our collapsed cores fit well with the stable soliton solution of the Schrödinger-Poisson equation, as shown in Fig. 3 (see also Supplementary Section 2 and Fig. S3). On the other hand, except for the lightest halo which has just formed and is not yet virialized, the outer profiles of other haloes possess a steepening logarithmic slope, similar to the Navarro-Frenk-White

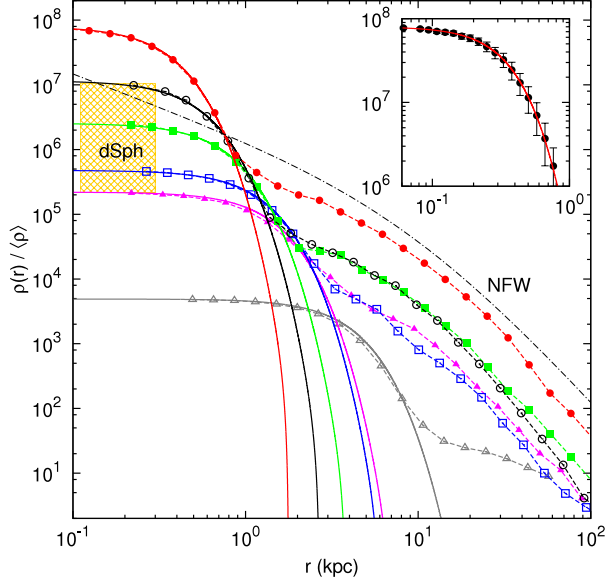


Figure 3: Radial density profiles of haloes formed in the ψ DM model. Dashed lines with various symbols show six examples of the halo profiles normalized to the cosmic mean density. All haloes are found to possess a distinct inner core fitted extremely well by the soliton solution (solid lines). A detailed soliton fit for the largest halo is inset, where the error is the root-mean-square scatter of density in each radial bin. An NFW profile representing standard CDM is also shown for comparison (black dot-dashed line, with a very large scale radius of 10 kpc), which fits well the profiles outside the cores. The yellow hatched area indicates the ρ_{300} of the dSph satellites around Milky Way^{2,22}, which is consistent with the majority of galaxy haloes formed in the ψ DM simulations.

(NFW) profile²³ of standard CDM. These solitonic cores, which are gravitationally self-bound and appear as additional mass clumps superposed on the NFW profile, are clearly distinct from the cores formed by WDM and collisional CDM which truncate the NFW cuspy inner profile at lower values and require an external halo for confinement. The radius of the soliton scales inversely with mass, such that the widest cores are the least massive and are hosted by the least massive galaxies. Eighty percent of the haloes in the simulation have an average density within 300 pc (defined as ρ_{300}) in the range $5.3 \times 10^{-3} - 6.1 \times 10^{-1} M_{\odot}/\text{pc}^3$, consistent with Milky Way satellites^{2,22}, and objects like these

are resilient to close interaction with massive galaxies. By contrast, the very lowest mass objects in our simulation have $\rho_{300} \sim 4.0 \times 10^{-4} M_{\odot}/\text{pc}^3$, but exist only briefly as they are vulnerable to tidal disruption by large galaxies in our simulations.

The prominent solitonic cores uncovered in our simulations provide an opportunity to estimate the boson mass, m_B , by comparison with observations, particularly for dSph galaxies where dark matter dominates. The local Fornax dSph galaxy is the best studied case with thousands of stellar velocity measurements, allowing a detailed comparison with our soliton mass profile. We perform a Jeans analysis for the dominant intermediate metallicity stellar population, which exhibits a nearly uniform projected velocity dispersion (σ_{\parallel})²⁴. We simultaneously reproduce well the radial distribution of the stars²⁴ (Fig. 4a) and their velocity dispersion with negligible velocity anisotropy, with $m_B = (8.1^{+1.6}_{-1.7}) \times 10^{-23}$ eV and core radius $r_c = 0.92^{+0.15}_{-0.11}$ kpc (see Supplementary Fig. S4). The corresponding core mass $M(r \leq r_c)$ is $\simeq 9.1 \times 10^7 M_{\odot}$, which is hosted by a halo with virial mass $\simeq 4 \times 10^9 M_{\odot}$ in the simulations. These results are similar to other estimates for Fornax^{4,25,26} (Fig. 4b) and consistent with other dSph galaxies derived by a variety of means^{3,25,27} (see Supplementary Section 3 for details).

For more massive galaxies, the solitons we predict are denser and more massive, scaling approximately as $M_s \simeq M_{gal}^{1/3}$. So for the Milky Way (MW), adopting a total mass of $M_{gal} = 10^{12} M_{\odot}$, we expect a soliton of $M_s \simeq 2 \times 10^9 M_{\odot}$, with core radius $\simeq 180$ pc and a potential depth corresponding to a line-of-sight velocity dispersion $\sigma_{\parallel} \simeq 115$ km/s for test particles satisfying the virial condition with the soliton potential. At face value this seems consistent with the MW bulge velocity dispersion where a distinctive flat peak is observed at a level of $\sigma_{\parallel} \simeq 110$ km/s within a projected radius ~ 200 pc^{29–31}. Such cores clearly have implications for the creation of spheroids acting as an essential seed for the prompt attraction of gas within a deepened potential. Indeed, bulge stars with $[\text{Fe}/\text{H}] > -1.0$ are firmly established as a uniformly old population that formed rapidly^{31,32}, a conclusion that standard Λ CDM struggles to explain via extended accretion and merging³¹. The implications for early spheroid formation and compact nuclear objects in general

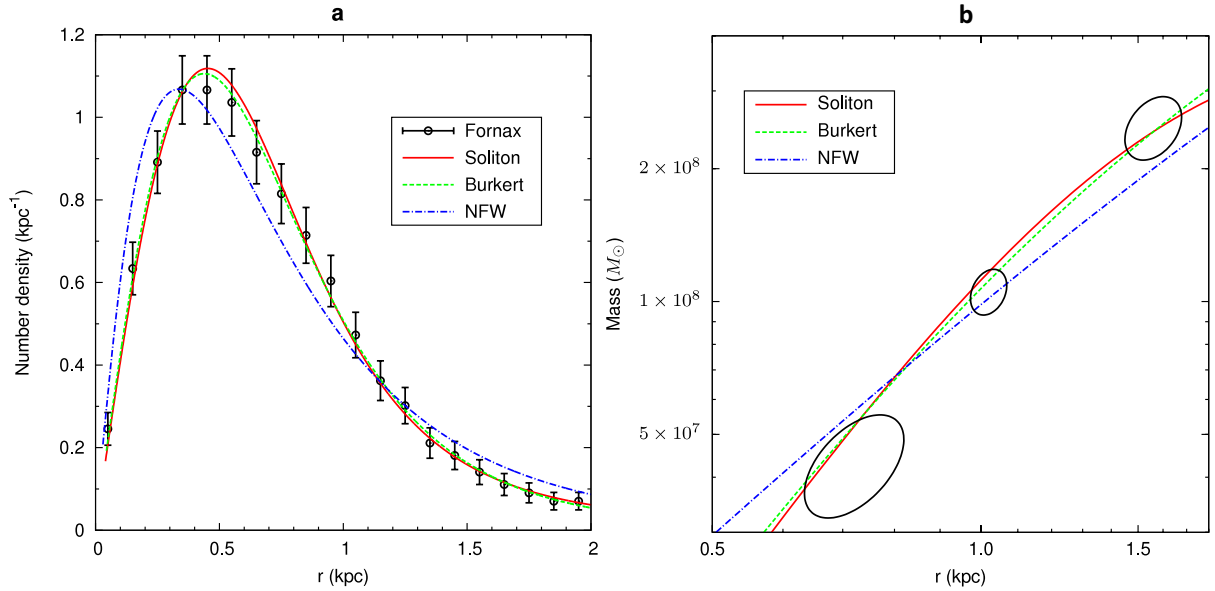


Figure 4: Modeling the Fornax dSph galaxy with the soliton profile. Panel (a) shows the normalized stellar number density of the intermediate metallicity subpopulation²⁴ (symbols with $1\text{-}\sigma$ error bars) and the best-fit soliton solution (red solid line) with $m_B = 8.1 \times 10^{-23}$ eV, $r_c = 0.92$ kpc, and $\sigma_{||} = 11.3$ km/s. Also shown are the best-fit empirical formula of Burkert²⁸ (green dashed line) and the NFW profile (blue dot-dashed line) representing standard CDM. The scale radius of NFW is restricted to be no larger than 3.0 kpc during the fit to exclude unreasonably small concentration parameters. Panel (b) shows the $1\text{-}\sigma$ contours of the total enclosed mass estimated from each of the three subpopulations⁴, overplotted with the model curves using the same best-fit parameters adopted in panel (a). Clearly, in both panels the soliton profile of ψ DM provides an accurate fit, matched only by the empirical fitting function of the Burkert profile, while NFW is not favoured by the data.

can be explored self-consistently with the addition of baryons to the ψ DM code, to model the interplay among stars, gas and ψ DM that will provide model rotation curves for an important test of this model.

At high redshift, the earliest galaxies formed from ψ DM are delayed relative to standard CDM, limited by the small amplitude of Jeans mass at radiation-matter equality, after which the first structures grow. This is demonstrated with a ψ DM simulation of a $30 \text{ h}^{-1} \text{ Mpc}$ box where we adopt $m_B = 8.1 \times 10^{-23}$ eV derived above. The first bound object collapses at $z \simeq 13$, with a clear solitonic core of mass $\simeq 10^9 M_\odot$ and radius $\simeq 300$ pc, whereas under Λ CDM the first objects should form at $z \simeq 50$ with masses of only $10^4 - 10^5 M_\odot$ ³³. The currently highest redshift galaxy at $z \simeq 10.7$ is multiply lensed, appearing smooth and spherical, with a stellar radius $\simeq 100$ pc³⁴, similar to local dSph galaxies. Deeper cluster lensing data from the Hubble “Frontier Fields” programme will soon meaningfully ex-

plore the mass limits of galaxy formation to higher redshift, allowing us to better distinguish between particle and wavelike cold dark matter.

References

1. Gilmore, G. *et al.* The observed properties of dark matter on small spatial scales. *Astrophys. J.* **663**, 948–959 (2007).
2. Strigari, L. E. *et al.* A common mass scale for satellite galaxies of the Milky Way. *Nature* **454**, 1096–1097 (2008).
3. Walker, M. G. & Peñarrubia, J. A method for measuring (slopes of) the mass profiles of dwarf spheroidal galaxies. *Astrophys. J.* **742**, 20–38 (2011).
4. Amorisco, N. C., Agnello, A. & Evans, N. W. The core size of the Fornax dwarf spheroidal. *Mon. Not. R. Astron. Soc.* **429**, L89–L93 (2013).

5. Kauffmann, G., White, S. D. M. & Guiderdoni, B. The formation and evolution of galaxies within merging dark matter haloes. *Mon. Not. R. Astron. Soc.* **264**, 201–218 (1993).
6. Klypin, A., Kravtsov, A. V., Valenzuela, O. & Prada, F. Where are the missing galactic satellites? *Astrophys. J.* **522**, 82–92 (1999).
7. Moore, B. *et al.* Dark matter substructure within galactic halos. *Astrophys. J.* **524**, L19–L22 (1999).
8. Peebles, P. J. E. Fluid dark matter. *Astrophys. J.* **534**, L127–L129 (2000).
9. Hu, W., Barkana, R. & Gruzinov, A. Fuzzy cold dark matter: the wave properties of ultra-light particles. *Phys. Rev. Lett.* **85**, 1158–1161 (2000).
10. Peebles, P. J. E. & Ratra, B. Cosmology with a time-variable cosmological ‘constant’. *Astrophys. J.* **325**, L17–L20 (1988).
11. Arvanitaki, A., Dimopoulos, S., Dubovsky, S., Kaloper, N. & March-Russell, J. String axiverse. *Phys. Rev. D* **81**, 123530 (2010).
12. Springel, V. The cosmological simulation code GADGET-2. *Mon. Not. R. Astron. Soc.* **364**, 1105–1134 (2005).
13. Widrow, L. M. & Kaiser, N. Using the Schroedinger equation to simulate collisionless matter. *Astrophys. J.* **416**, L71–L74 (1993).
14. Sikivie, P. & Yang, Q. Bose-Einstein condensation of dark matter axions. *Phys. Rev. Lett.* **103**, 111301 (2009).
15. Woo, T.-P. & Chiueh, T. High-resolution simulation on structure formation with extremely light bosonic dark matter. *Astrophys. J.* **697**, 850–861 (2009).
16. Spergel, D. N. & Steinhardt, P. J. Observational evidence for self-interacting cold dark matter. *Phys. Rev. Lett.* **84**, 3760–3763 (2000).
17. Bode, P., Ostriker, J. P. & Turok, N. Halo formation in warm dark matter models. *Astrophys. J.* **556**, 93–107 (2001).
18. Strigari, L. E. *et al.* A large dark matter core in the Fornax dwarf spheroidal galaxy? *Astrophys. J.* **652**, 306–312 (2006).
19. Macciò, A. V., Paduroiu, S., Anderhalden, D., Schneider, A. & Moore, B. Cores in warm dark matter haloes: a Catch 22 problem. *Mon. Not. R. Astron. Soc.* **424**, 1105–1112 (2012).
20. Rocha, M. *et al.* Cosmological simulations with self-interacting dark matter - I. Constant-density cores and substructure. *Mon. Not. R. Astron. Soc.* **430**, 81–104 (2013).
21. Schive, H.-Y., Tsai, Y.-C. & Chiueh, T. GAMER: a graphic processing unit accelerated adaptive-mesh-refinement code for astrophysics. *Astrophys. J. Suppl.* **186**, 457–484 (2010).
22. Amorisco, N. C. & Evans, N. W. Phase-space models of the dwarf spheroidals. *Mon. Not. R. Astron. Soc.* **411**, 2118–2136 (2011).
23. Navarro, J. F., Frenk, C. S. & White, S. D. M. The structure of cold dark matter halos. *Astrophys. J.* **462**, 563–575 (1996).
24. Amorisco, N. C. & Evans, N. W. A troublesome past: chemodynamics of the Fornax dwarf spheroidal. *Astrophys. J.* **756**, L2–L6 (2012).
25. Wolf, J. *et al.* Accurate masses for dispersion-supported galaxies. *Mon. Not. R. Astron. Soc.* **406**, 1220–1237 (2010).
26. Cole, D. R., Dehnen, W., Read, J. I. & Wilkinson, M. I. The mass distribution of the Fornax dSph: constraints from its globular cluster distribution. *Mon. Not. R. Astron. Soc.* **426**, 601–613 (2012).
27. Lora, V., Magaña, J., Bernal, A., Sánchez-Salcedo, F. J. & Grebel, E. K. On the mass of ultra-light bosonic dark matter from galactic dynamics. *J. Cosmol. Astropart. Phys.* **2**, 11–32 (2012).
28. Burkert, A. The structure of dark matter halos in dwarf galaxies. *Astrophys. J.* **447**, L25–L28 (1995).
29. Minniti, D. Field stars and clusters of the Galactic bulge: implications for galaxy formation. *Astrophys. J.* **459**, 175–180 (1996).
30. Rich, R. M., Reitzel, D. B., Howard, C. D. & Zhao, H. The bulge radial velocity assay: techniques and a rotation curve. *Astrophys. J.* **658**, L29–L32 (2007).
31. Ness, M. *et al.* ARGOS - IV. The kinematics of

- the Milky Way bulge. *Mon. Not. R. Astron. Soc.* **432**, 2092–2103 (2013).
32. Zoccali, M. *et al.* Age and metallicity distribution of the Galactic bulge from extensive optical and near-IR stellar photometry. *Astron. & Astrophys.* **399**, 931–956 (2003).
 33. Abel, T., Bryan, G. L. & Norman, M. L. The formation of the first star in the universe. *Science* **295**, 93–98 (2002).
 34. Coe, D. *et al.* CLASH: three strongly lensed images of a candidate $z \approx 11$ galaxy. *Astrophys. J.* **762**, 32–52 (2013).

Acknowledgements We thank Tak-Pong Woo for calculating the soliton solution and Ming-Hsuan Liao for helping conduct the simulations. The GPU cluster donated by Chipbond Technology Corporation, with which this work is conducted, is acknowledged. This work is supported in part by the National Science Council of Taiwan under the grants NSC100-2112-M-002-018-MY3 and NSC99-2112-M-002-009-MY3.

Supplementary Information

Hsi-Yu Schive¹, Tzihong Chiueh^{1,2*} & Tom Broadhurst^{3,4}

chiuehth@phys.ntu.edu.tw

This document provides supplementary information for the letter. We begin by summarizing our simulation method, then we describe the soliton solution of the Schrödinger-Poisson equation and finally, we test the soliton solution against the observed internal stellar dynamics of dSph galaxies and constrain the boson mass m_B of the ψ DM model.

Simulation method

The governing equation in the ψ DM model is the Schrödinger-Poisson (SP) equation, expressed here in the comoving coordinates;

$$\left[i \frac{\partial}{\partial \tau} + \frac{\nabla^2}{2} - aV \right] \psi = 0 \quad (1)$$

and

$$\nabla^2 V = |\psi|^2 - 1, \quad (2)$$

where a is the cosmic scale factor and V is the gravitational potential. The comoving coordinates are normalized to the length $\xi \equiv (\frac{3}{2}H_0^2\Omega_{m0})^{1/4}(m_B/\hbar)^{1/2}\mathbf{x}$ and the normalized timestep $d\tau \equiv (\frac{3}{2}H_0^2\Omega_{m0})^{1/2}a^{-2}dt$, where H_0 is the present Hubble parameter, Ω_{m0} the present dark matter density parameter, and m_B the particle mass. The comoving mass density $\rho = |\psi|^2$ is normalized to the comoving background density $\langle \rho \rangle$.

In earlier work we adopted a pseudospectral method to simulate the ψ DM model with a uniform mesh resolution¹, but the spatial resolution achieved (1024^3 grid) was inadequate for the innermost regions of the haloes. To form a minimum of a few tens of dSph mass objects, the simulation volume must span a few cubic Mpc. On the other hand, to be capable of resolving the compact cores with sizes of few hundreds pc that we find forming within each halo, the spatial resolution must achieve at least few tens pc. Hence the dynamical range in scale is $\sim 10^5$, which is infeasible with a uniform mesh.

To solve this issue, we have developed a highly optimized AMR framework, GAMER^{2,3}, featuring an extremely efficient solution to integrating the AMR method with graphic processing units (GPUs) for computation acceleration. We incorporate an oct-tree AMR algorithm⁴, and use CPUs to manipulate the AMR data structure and GPUs to accelerate the partial differential equation solvers for the SP equation. To optimize the simulation performance, we implement the asynchronous data transfer between CPUs and GPUs and the hybrid MPI/OpenMP/GPUs parallelization, and fully exploit the simultaneity of CPUs' and GPUs' computation. The workload balance among multiple GPUs is achieved by the Hilbert space-filling curve method. As a result, an overall performance speedup up to 40 has been demonstrated in various GPU clusters for the ψ DM simulations.

We advance the wave function forward in time by applying a unitary transformation $\psi(\tau + \Delta\tau) = e^{-iW\Delta\tau}e^{-iK\Delta\tau}\psi(\tau)$, which is an approximate solution to the SP equation when the evolution timestep $\Delta\tau$ is small. Here $K (\equiv -\nabla^2/2)$ and $W (\equiv aV)$ are the kinematic and potential energy operators, respec-

¹Dept. of Physics, National Taiwan Univ., Taipei 10617, Taiwan

²Center for Theoretical Sciences, National Taiwan Univ., Taipei 10617, Taiwan

³Dept. of Theoretical Physics, Univ. of the Basque Country UPV/EHU, E-48080 Bilbao, Spain

⁴Ikerbasque, Basque Foundation for Science, E-48011 Bilbao, Spain

tively. The unitary operator $e^{-iK\Delta\tau}$ is expanded explicitly to order $\Delta\tau^{N_K}$. From the von Neumann stability analysis⁵ we find that $N_K \leq 2$ is unconditionally unstable. In practice, we choose $N_K = 5$ with modified Taylor expansion coefficients in order to minimize the small-scale numerical damping. The gravitational potential is calculated via a multi-level Poisson solver, where the Fast Fourier Transform (FFT)⁶ method with periodic boundary condition is applied at the AMR root level (the lowest resolution level covering the entire simulation volume). Either the successive overrelaxation (SOR) or the multigrid Poisson solver⁵ is adopted at the refinement levels. Second-order accuracy has been verified in a variety of tests. Technicalities of the numerical schemes are to be detailed in a separate paper (Schive et al., in preparation).

The evolution timesteps are determined by $d\tau \leq \min[4C_K\Delta\xi^2/(3\pi), 2\pi C_W/(a|V|_{\max})]$, where the two terms in the square bracket stem from the stability consideration of K and W operators, respectively. Here $C_K (= 0.625)$ and $C_W (= 0.3)$ are parameters controlling the integration accuracy. Having $C_K \leq 1.0$ and $C_W \leq 1.0$ ensures that the phase angle of wave function rotated in one timestep is smaller than 2π . Note that the kinematic solver requires $d\tau \propto \Delta\xi^2$, a signature of the ∇^2 operator. This unpleasant scaling leads to an extremely small timestep ($\Delta a \sim 1 \times 10^{-6}$) when high spatial resolution ($\sim 10^2$ pc) is required. To alleviate this issue, we have adopted the individual timestep scheme, with which lower resolution regions are allowed to have larger timesteps and the smallest timestep is applied only to the highest resolution regions, normally occupying less than 1% of the entire simulation volume.

Upon simulating the wave mechanics, the grid refinement criteria need to be carefully designed in order to achieve appropriate resolution everywhere. In particular, since the flow velocity can be expressed as $\mathbf{v} \equiv \nabla S$, where we let $\psi \equiv f e^{iS}$, the wave function will exhibit strong and rapid oscillation in the regions with high velocity. Therefore, unlike the conventional CDM simulations with AMR, where in general higher spatial resolution is required only around the regions with higher density or density contrast, here we also need sufficient spatial and temporal resolution to resolve the high-speed flow, even if the

density is low and smooth (Fig. S1). However, using flow velocity \mathbf{v} directly as the refinement criterion is impractical since \mathbf{v} is not an observable and may also diverge (e.g., in the locations of zero density resulting from interference). To solve the issue, we have applied the Löhner's error estimator⁷, which basically estimates the ratio between the second and first derivatives of both the real and imaginary parts of the wave function. Specifically, we demand there should be at least four cells to resolve one wavelength. In addition, we prohibit grid refinement in regions of extremely low density, where quantized vortices can form^{8,9} but are not relevant to this work. Finally, any cell with enclosed mass larger than $1.5 \times 10^5 M_\odot$ (which is equal to $8\langle\rho\rangle\Delta\xi_0^3$, where $\Delta\xi_0$ is the root-level cell size) is forced to be refined so as to capture the core structure.

The volume of our detailed simulation is 2 Mpc on a side, with a base-level grid $N = 256^3$ and up to seven refinement levels, giving an effective resolution 60 pc. The initial linear power spectrum was constructed by CMBFAST¹⁰ in a Λ CDM universe at $z = 1,000$, with cosmological parameters consistent with the recent observation¹¹. The relatively high initial redshift adopted here compared with traditional CDM simulations ensures substantial high- k damping of $\sim 10^3$ in the linear power spectrum when reaching $z \sim 30$ (Fig. S2). Note that in our comparison of ψ DM and particle CDM evolution, shown in Fig. 1, we scale the ψ DM linear power spectrum at $z = 30$ back to $z = 100$ as the initial condition for particle CDM simulation in order to highlight the large-scale features.

Soliton solution

A soliton solution to the SP equation can be found numerically as follows. Firstly, when deriving the soliton profile, it is reasonable to assume $a = 1$ and $|\psi|^2 \gg 1$ in Eqs. (1) and (2) even in a cosmological context since the characteristic wave crossing time around the core is much shorter than the Hubble time and the core density is at least several orders of magnitude higher than the background density. Then, by assuming spherical symmetry and inserting the stationary condition $\psi(\xi, \tau) = e^{-i\omega\tau}\Psi(\xi)$, the dimensionless SP equation can be further reduced to a coupled second-order ordinary differential equation that can be solved numerically with proper

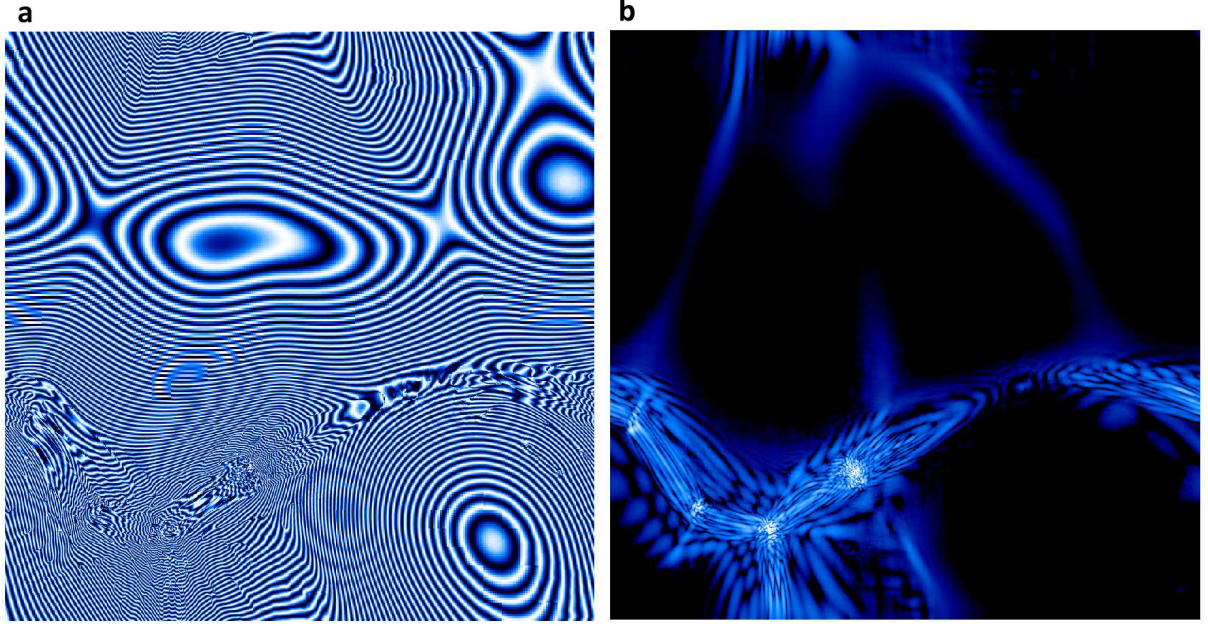


Figure S1: Square wave function $\psi^2 (\equiv f^2 e^{i2S})$ in the ψ DM simulation. Panels (a) and (b) show a 2 Mpc slice of phase ($\sin(2S)$) and amplitude (f^2) of the wave function at $z = 3.1$, respectively. The simulation challenge arises from the complexity of the wave function. Strong and rapid phase oscillations are common everywhere (even in the low-density background shown by the dark regions in the density plot), where sufficient spatial and temporal resolution is required to resolve each wavelength.

boundary conditions¹². The soliton profile is close to Gaussian, with a near constant-density core and a steeper outer gradient (Fig. S3). We define a core radius r_c at which the density has dropped to one-half its peak value. The corresponding core mass $M_c \equiv M(r \leq r_c)$ encloses roughly 1/4 of the total soliton mass $M_s \equiv M(r \rightarrow \infty)$. The half-mass radius is $\sim 1.45 r_c$.

An important feature of the soliton solution to appreciate is its scaling symmetry¹². The wave function and the associated physical quantities allow for a scale transformation, $(r, \psi, \rho_s, M_s) \rightarrow (\lambda^{-1} r, \lambda^2 \psi, \lambda^4 \rho_s, \lambda M_s)$, where ρ_s is the soliton density profile, to generate other solutions, thus forming a one-parameter family. Accordingly, all soliton solutions can be characterised by a single parameter (for example, r_c), providing clear predictions for the correlation between different core properties. For example, if the core radius of a galaxy is observed to be half the size of another, the soliton solution predicts the core mass and peak density to be two and sixteen times higher.

The soliton profile does not have an analytical

form and the solution can only be obtained numerically. But thanks to the scaling symmetry, the core mass and core radius obey a simple relation

$$M_c \approx \frac{5.5 \times 10^9}{(m_B/10^{-23} \text{ eV})^2 (r_c/\text{kpc})} M_\odot. \quad (3)$$

For example, with the best-fit for Fornax of $m_B = 8.1 \times 10^{-23} \text{ eV}$ and $r_c = 0.92 \text{ kpc}$, we readily have $M_c \sim 9.1 \times 10^7 M_\odot$ and $M_s \sim 3.6 \times 10^8 M_\odot$. In addition, it is found that within the range $0 \leq r \lesssim 3 r_c$, which encloses $\sim 95\%$ of the total soliton mass, the soliton density profile can be well approximated by

$$\rho_s(r) \approx \frac{1.9 (m_B/10^{-23} \text{ eV})^{-2} (r_c/\text{kpc})^{-4}}{[1 + 9.1 \times 10^{-2} (r/r_c)^2]^8} M_\odot \text{pc}^{-3}, \quad (4)$$

which is consistent with the scaling relation that the peak density is proportional to r_c^{-4} for a given particle mass. This approximate analytical formula makes it convenient to compare the soliton model and observation, from which the best-fit m_B and r_c can be determined (see the next section).

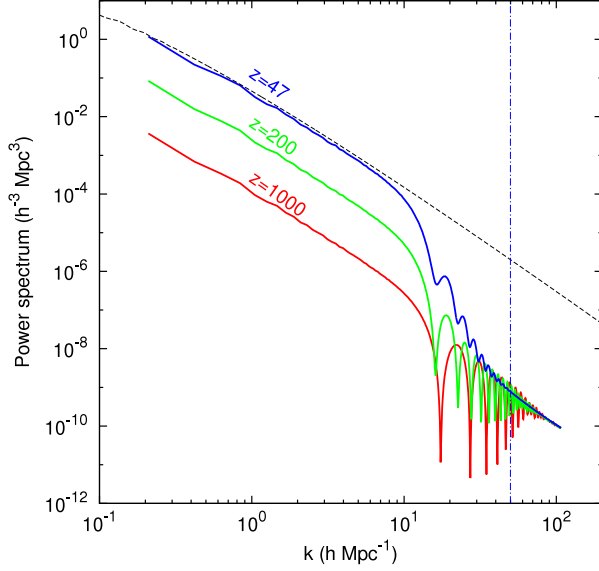


Figure S2: Dark matter power spectrum at various epochs. Solid lines show the power spectra obtained for the ψ DM model with a $30 \text{ h}^{-1} \text{ Mpc}$ simulation box and 1024^3 resolution, and the vertical dot-dashed line shows the Jeans length at $z = 47$. The dashed line denotes the predicted linear power spectrum in the conventional CDM model at $z = 47$.

Data modeling

The dSph galaxies are the most dark-matter dominated objects known, as indicated from their high mass-to-light ratios and hence very useful for determining the properties of dark matter on small scales. By assuming spherical symmetry and dynamical equilibrium, the total mass profile $M(r)$ can be related to the observed distribution of stars and their velocity dispersion profile via the Jeans equation¹³:

$$\frac{d(\rho_* \sigma_r^2)}{dr} = -\rho_* \frac{d\Phi}{dr} - \frac{2\beta \rho_* \sigma_r^2}{r}, \quad (5)$$

where $\rho_*(r)$ is the stellar density, $\sigma_r(r)$ describes the radial velocity dispersion, $\beta(r)$ quantifies the stellar velocity anisotropy, and $\Phi(r)$ is the gravitational potential satisfying $d\Phi/dr = GM(r)/r^2$. For the observed line-of-sight velocity dispersion profile and the projected stellar distribution, one can then parameterise $\rho_*(r)$, $\beta(r)$, $M(r)$ and determine the best fit to the data. Unfortunately, none of the mass models adopted in previous work resemble the soliton profile found in the ψ DM model.

We first examine the well studied Fornax dSph

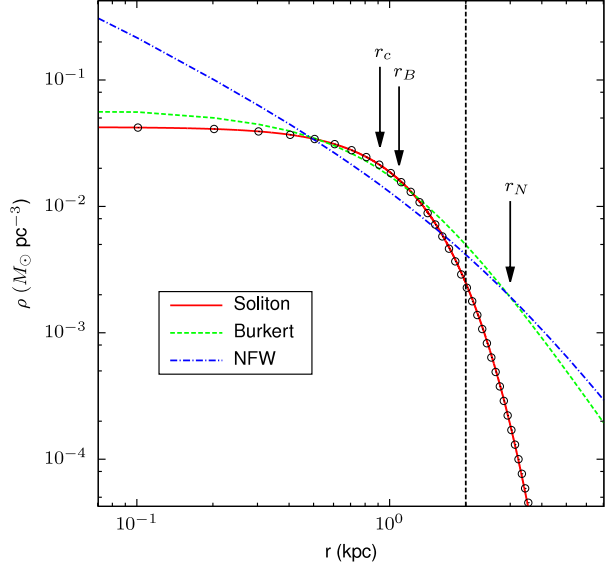


Figure S3: Soliton density profile. The red solid line shows the numerical solution, and circles show the approximate analytical form (Eq. [4]) found to fit well to the soliton profile within $3r_c$. For comparison, we also show the empirically motivated Burkert (green dashed line) and NFW (blue dot-dashed line) profiles. All three model curves are plotted using the best-fit parameters to Fornax, and the vertical dashed line represents the upper limit of radius adopted for the fitting. Arrows indicate the soliton core radius (r_c), the scale radius of Burkert (r_B), and NFW (r_N), respectively.

galaxy as a benchmark. Fornax is found to have three stellar subpopulations inferred from their different metallicities, kinematics, and spatial distribution¹⁴. Although these subpopulations reside in the same gravitational potential, they have different half-light radii and hence sample different volumes of the core. The predominant intermediate metallicity subpopulation has a projected half-light radius $R_h \sim 0.61 \text{ kpc}$ and a nearly constant line-of-sight velocity dispersion $\sigma_{||} \sim 11.3 \pm 0.7 \text{ km/s}$ within $0 \leq r \lesssim 1.4 \text{ kpc}$, indicative of an isotropic velocity dispersion ($\beta \sim 0$). The simplicity of this subpopulation leads to an exact solution to Eq. (5), $\rho_*(r) = \rho_0 \exp[-\phi(r)/\sigma_r^2]$, allowing us to determine the stellar density beyond the half-light radius. By making a further assumption that the stellar self-gravity is negligible, the gravitational potential $\phi(r)$ of dark matter can be calculated analytically from Eq. (4) for a given particle mass and core radius, which we show in Fig. S4 for a

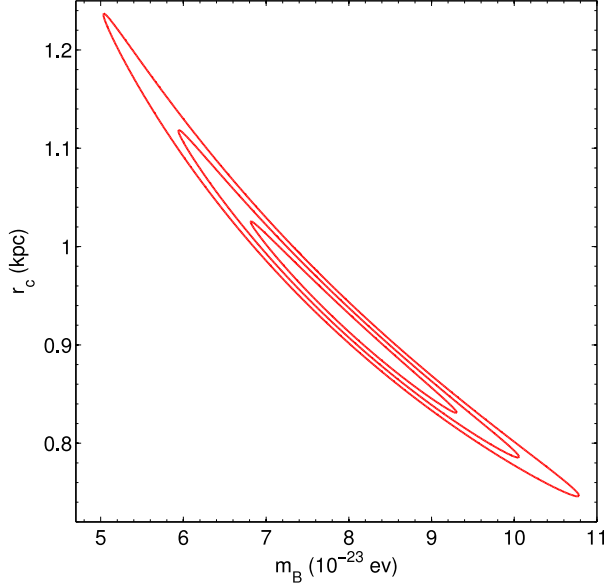


Figure S4: Confidence regions of the dark matter mass and core radius for the soliton profile fit to Fornax. Contours show the regions of 68%, 95%, and 99.7% confidence, respectively.

range of confidence levels.

Notice the tight correlation between m_B and r_c shown in Fig. S4, namely $m_B \propto r_c^{-1.5}$. This results from the fact that nearly two-third of the stars used in this fit are located inside the core radius, by which only the peak core density is constrainable, with m_B and r_c to be degenerate in this limit as $m_B \propto r_c^{-2}$ (referred to Eq. [4]). Nevertheless, one third of the stars still lie outside the core radius so that the degeneracy between m_B and r_c is broken to some degree. By comparison, the metal-rich subpopulation is more concentrated inside the core, from which m_B and r_c will be poorly constrained individually.

In the following we describe several consistency checks for the m_B and r_c determined above. Firstly, the three separate stellar subpopulations of Fornax also provide three independent enclosed mass estimates along the mass profile of Fornax^{15,16}. Each stellar subpopulation has a different half-light radius, $R_h \sim 430 - 940$ pc, and velocity dispersion, $\sigma_{||} \sim 7 - 17$ km/s, for which the enclosed mass can be related to mean radius by a model-independent expression $M(1.67 R_h) \simeq 5.85 R_h \sigma_{||}^2(R_h)/G$ - a simple well tested relation^{17,18}. The consistency between the soliton and Fornax mass profiles is veri-

fied within the $1-\sigma$ confidence region for each point (see Fig. 4b), although the soliton mass profile is a bit higher at $r \sim 1$ kpc. It is worthwhile to note that the metal-poor subpopulation has the largest mean radius, $R_h \sim 935$ pc, providing a mass estimate for $r \sim 1.6$ kpc which is greatly beyond the core radius. This subpopulation therefore provides a strong constraint on the density profile outside the constant-density region and substantially breaks the $m_B - r_c$ degeneracy.

The existence of five old globular clusters in Fornax provides another evidence for the large core^{19,20}. These globular clusters reside at ~ 1 kpc in radius from the centre of Fornax and their dynamical friction timescale is determined from N-body calculations to be far shorter than the Hubble time, so that these clusters should be found at the centre of Fornax if the density profile of Fornax followed the predicted cuspy form of particle CDM. Instead, for these objects to be dynamically stable at their observed radii, a cored profile is indicated, of a similar radius again consistent with our predicted core radius for Fornax.

Stars in the Sculptor dSph have also been reliably separated by metallicity into metal-rich and metal-poor subpopulations^{15,18}. Enclosed masses of the two subpopulations have been determined to be $M(r \lesssim 167 \text{ pc}) \sim 4.1 \times 10^6 M_\odot$ and $M(r \lesssim 302 \text{ pc}) \sim 2.4 \times 10^7 M_\odot$, respectively¹⁵. It is found that $M(r) \propto r^3$, indicative of both subpopulations residing well within a flat core, thus preventing us from constraining m_B and r_c separately. On the other hand, by comparing with the mass density of Fornax and using the soliton density scaling $\rho(r=0) \propto r_c^{-4}$, we estimate the core size of Sculptor to be ~ 610 pc, verifying that the two subpopulations are indeed well within the core.

A third dSph galaxy that favors the cored dark matter profile in the literature is Ursa Minor^{21,22}, which is one of the most dark-matter dominated classical Milky Way dwarf satellites, with a mass-to-light ratio $\sim 70 M_\odot/L_\odot$. A kinematically cold, and dense old star cluster is found in Ursa Minor, and it was shown by N-body simulations that such a cold clump can be easily destroyed within less than 1 Gyr in a cuspy density profile, hence incompatible with the standard CDM model. By comparison, it was demonstrated that the cold substructure can be stable

for a Hubble time if residing in a harmonic dark matter potential of a flat cored profile with $r_c \gtrsim 450$ pc. To check whether it accords with our best-fit soliton model, we take $M(r < 280 \text{ pc}) = 1.3 \times 10^7 M_\odot$ ¹⁷ and assume this mass to be well within the core, from which we estimate $r_c \sim 680$ pc, consistent with the core size estimated by other studies.

References

1. Woo, T.-P. & Chiueh, T. High-resolution simulation on structure formation with extremely light bosonic dark matter. *Astrophys. J.* **697**, 850–861 (2009).
2. Schive, H.-Y., Tsai, Y.-C. & Chiueh, T. GAMER: a graphic processing unit accelerated adaptive-mesh-refinement code for astrophysics. *Astrophys. J. Suppl.* **186**, 457–484 (2010).
3. Schive, H.-Y., Zhang, U.-H. & Chiueh, T. Directionally unsplit hydrodynamic schemes with hybrid MPI/OpenMP/GPU parallelization in AMR. *Int. J. High Perform. Comput. Appl.* **26**, 367–377 (2012).
4. MacNeice, P., Olson, K. M., Mobarry, C., de Fainchtein, R. & Packer, C. PARAMESH: a parallel adaptive mesh refinement community toolkit. *Comp. Phys. Comm.* **126**, 330–354 (2000).
5. Press, W. H., Teukolsky, S. A., Vetterling, W. T. & Flannery, B. P. *Numerical Recipes. The Art of Scientific Computing* (Cambridge Univ. Press, Cambridge, 2007).
6. Frigo, M. & Johnson, S. G. The design and implementation of FFTW3. *Proceedings of the IEEE* **93**, 216–231 (2005).
7. Löhner, R. An adaptive finite element scheme for transient problems in CFD. *Comput. Methods Appl. Mech. Eng.* **61**, 323–338 (1987).
8. Chiueh, T. Dynamical quantum chaos as fluid turbulence. *Phys. Rev. E* **57**, 4150–4154 (1998).
9. Chiueh, T., Woo, T.-P., Jian, H.-Y. & Schive, H.-Y. Vortex turbulence in linear Schrödinger wave mechanics. *J. Phys. B: At. Mol. Opt. Phys.* **44**, 115101 (2011).
10. Seljak, U. & Zaldarriaga, M. A line-of-sight integration approach to cosmic microwave background anisotropies. *Astrophys. J.* **469**, 437–444 (1996).
11. Hinshaw, G. *et al.* Nine-year Wilkinson Microwave Anisotropy Probe (WMAP) observations: cosmological parameter results. *Astrophys. J. Suppl.* in press (available at <http://www.arxiv.org/abs/1212.5226>).
12. Guzmán, F. S. & Ureña-López, L. A. Gravitational cooling of self-gravitating Bose condensates. *Astrophys. J.* **645**, 814–819 (2006).
13. Binney, J. & Tremaine, S. *Galactic Dynamics* (Princeton Univ. Press, Princeton, 2008).
14. Amorisco, N. C. & Evans, N. W. A troublesome past: chemodynamics of the Fornax dwarf spheroidal. *Astrophys. J.* **756**, L2–L6 (2012).
15. Walker, M. G. & Peñarrubia, J. A method for measuring (slopes of) the mass profiles of dwarf spheroidal galaxies. *Astrophys. J.* **742**, 20–38 (2011).
16. Amorisco, N. C., Agnello, A. & Evans, N. W. The core size of the Fornax dwarf spheroidal. *Mon. Not. R. Astron. Soc.* **429**, L89–L93 (2013).
17. Walker, M. G. *et al.* A universal mass profile for dwarf spheroidal galaxies? *Astrophys. J.* **710**, 886–890 (2010).
18. Amorisco, N. C. & Evans, N. W. Dark matter cores and cusps: the case of multiple stellar populations in dwarf spheroidals. *Mon. Not. R. Astron. Soc.* **419**, 184–196 (2012).
19. Goerdt, T., Moore, B., Read, J. I., Stadel, J. & Zemp, M. Does the Fornax dwarf spheroidal have a central cusp or core? *Mon. Not. R. Astron. Soc.* **368**, 1073–1077 (2006).
20. Cole, D. R., Dehnen, W., Read, J. I. & Wilkinson, M. I. The mass distribution of the Fornax dSph: constraints from its globular cluster distribution. *Mon. Not. R. Astron. Soc.* **426**, 601–613 (2012).
21. Kleyna, J. T., Wilkinson, M. I., Gilmore, G. & Evans, N. W. A dynamical fossil in the Ursa Minor dwarf spheroidal galaxy. *Astrophys. J.* **588**, L21–L24 (2003).
22. Lora, V., Magaña, J., Bernal, A., Sánchez-

Salcedo, F. J. & Grebel, E. K. On the mass of ultra-light bosonic dark matter from galactic dynamics. *J. Cosmol. Astropart. Phys.* **2**, 11–32 (2012).